Chemical Physics 442 (2014) 137–142

Contents lists available at ScienceDirect

Chemical Physics

journal homepage: www.elsevier.com/locate/chemphys

# Sub-100-ps structural dynamics of horse heart myoglobin probed by time-resolved X-ray solution scattering

Key Young Oang [a,b], Kyung Hwan Kim [a,b], Junbeom Jo [a,b], Youngmin Kim [a,b], Jong Goo Kim [a,b], Tae Wu Kim [a,b], Sunhong Jun [a,b], Jeongho Kim [c], Hyotcherl Ihee [a,b,*]

[a] Center for Nanomaterials and Chemical Reactions, Institute for Basic Science (IBS), Daejeon 305-701, Republic of Korea
[b] Department of Chemistry, Graduate School of Nanoscience & Technology (WCU), KAIST, Daejeon 305-701, Republic of Korea
[c] Department of Chemistry, Inha University, Incheon 402-751, Republic of Korea

ARTICLE INFO

*Article history:*
Available online 2 April 2014

*Keywords:*
Time-resolved X-ray solution scattering
Time-slicing
Structural dynamics
Myoglobin

ABSTRACT

Here we report sub-100-ps structural dynamics of horse heart myoglobin revealed by time-resolved X-ray solution scattering. By applying the time-slicing scheme to the measurement and subsequent deconvolution, we investigate the protein structural dynamics that occur faster than the X-ray temporal pulse width of synchrotrons (~100 ps). The singular value decomposition analysis of the experimental data suggests that two structurally distinguishable intermediates are formed within 100 ps. In particular, the global structural change occurring on the time scale of 70 ps is identified.



## 1. Introduction

Determining three-dimensional structures of intermediates involved in a protein transition is important for an understanding of the relationship between structure, dynamics, and function of the proteins. Since proteins undergo structural transitions on a wide range of time scales (from sub-picoseconds to seconds) and length scales (from sub-angstroms to tens of angstroms), characterization of the protein intermediates calls for an experimental tool that has high spatiotemporal resolution. In particular, intermediates formed at the earliest stage of the protein transition need to be characterized because they trigger large-amplitude earthquake in the whole protein matrix. Over the last decade, time-resolved X-ray solution scattering based on the 3rd-generation light source (synchrotron) has revealed structural dynamics of various reactions of small molecules and biological macromolecules in solution phase [1–38]. They include diatomic and triatomic molecules ($I_2$, $Br_2$, $HgI_2$, $HgBr_2$, and $I_3^-$), haloalkanes ($CBr_4$, $CHI_3$, $CH_2I_2$, $C_2H_4I_2$, and $C_2F_4I_2$), organometallic compounds ($Ru_3(CO)_{12}$, $Os_3(CO)_{12}$, $[Ir_2(dimen)_4]^{2+}$, $[Fe(bpy)_3]^{2+}$, *cis*-$[Ru(bpy)_2(py)_2]^{2+}$ and $[Pt_2(P_2O_5H_2)_4]^{4-}$), nanoparticles, and protein molecules (myoglobin, hemoglobin, homodimeric hemoglobin, photoactive yellow protein, cytochrome-c, and proteorhodopsin). Since all of those previous studies were investigated with the time resolution of 100 ps at best, there remain many issues waiting for investigation on earlier time scale using femtosecond X-ray pulses from the 4th-generation light source (XFEL).

As a step towards this goal, here we present a time-resolved X-ray solution scattering experiment on a protein using a time-slicing scheme. In the time-slicing scheme described in Fig. 1, we measure time-resolved X-ray solution scattering data while varying the temporal delay between laser and X-ray pulses with fine increments (10 ps) around time zero ($\Delta t$ = 0 ps). Then, we deconvolute the temporal profile of the X-ray pulse from the measured data to extract dynamics occurring earlier than the time resolution of the experiment (100 ps). Recently, we used this time-slicing approach to investigate the reaction dynamics of $I_2$ molecules, and visualized geminate recombination and vibrational relaxation of $I_2$ molecules and accompanying solvent rearrangement [27]. In this work, we extend the time-slicing scheme to a protein, horse heart myoglobin (Mb), to capture sub-100-ps structural dynamics of the protein.

Horse heart Mb is a heme protein that can bind small-molecule ligands such as $O_2$ and CO and has served as a prototypical model system for studying protein structural dynamics [21,39–45]. So far, early-time dynamics of horse heart Mb in solution initiated by ligand photodissociation have been studied mainly by time-resolved optical spectroscopies due to their superb time resolution [41–45]. Although the optical spectroscopic tools have been quite successful in identifying the time scales for the formation of intermediates involved in protein transitions, their signals are not directly related to three-dimensional structure of the protein. Alternatively,

* Corresponding author at: Department of Chemistry, KAIST, Daejeon 305-701, Republic of Korea. Tel.: +82 423502844; fax: +82 423502810.
*E-mail address:* hyotcherl.ihee@kaist.ac.kr (H. Ihee).

http://dx.doi.org/10.1016/j.chemphys.2014.03.004
0301-0104/

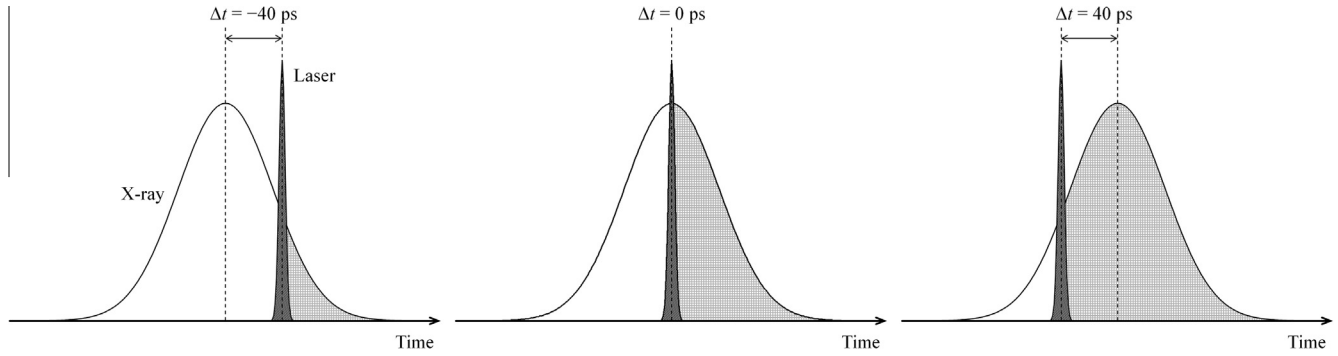


**Fig. 1.** Principle of the time-slicing measurement. At a negative time delay around time zero (for example −40 ps; left), the laser pulse arrives later than the center of the X-ray pulse at the sample position. However, the X-ray pulse has much larger pulse width than the laser pulse and is still present after the ligand photodissociation of horse heart MbCO induced by the laser pulse. Therefore, a small portion of the X-ray pulse is scattered from the photoexcited sample that undergoes global structural changes. At time zero (middle), half of the X-ray pulse is scattered from the photoexcited sample. At a positive time delay (for example +40 ps; right), more than half of the X-ray pulse is scattered from the photoexcited sample.

time-resolved Laue crystallography can provide a combination of high time resolution and structural sensitivity [46–51], but it requires the preparation of highly-ordered and radiation–resistant single crystals, limiting its applicability to only a few model systems. More importantly, the protein motions in crystalline sample might be different from those in physiological aqueous environment where proteins actually perform their functions [48–50].

In this regard, time-resolved X-ray solution scattering is a perfect tool to circumvent these limitations of optical spectroscopy and Laue crystallography. For example, the difference between X-ray solution scattering curve of horse heart Mb liganded with CO molecules (MbCO) and that of horse heart Mb measured at 100 ps after the ligand photodissociation clearly exhibits highly oscillatory features [21]. Considering that crystallographic structural models of liganded and unliganded horse heart Mb are different from each other only slightly with RMSD values less than 0.3 Å [39], the nonzero difference clearly demonstrates high structural sensitivity of time-resolved X-ray solution scattering. Furthermore, the appearance of the difference at 100 ps after the ligand photodissociation, which is the time resolution of the experiment at synchrotrons, suggests that significant structural change occurs faster than 100 ps. Thus, in this work, we focus on elucidating sub-100-ps structural dynamics of horse heart Mb in solution using time-resolved X-ray solution scattering combined with the time-slicing scheme.

## 2. Experimental section

Time-resolved X-ray solution scattering data were measured at the BioCARS 14-ID-B beamline at the Advanced Photon Source (APS) while the storage ring was operated in the top-up mode at 7 GeV [52]. The X-ray spectrum, which is peaked at 12 keV with a long wavelength tail, has the bandwidth of ~3%. The full spectrum was used without being monochromatized to reduce the data collection time. The blurring effect of the polychromaticity with ~3% bandwidth to the scattering curve is insignificant. The 80-ps-long (FWHM) X-ray pulse containing $\sim 10^{10}$ photons was transferred to the sample position with a spot size of $0.09 \times 0.06$ mm$^2$ (horizontal × vertical, FWHM). A heat-load chopper, a Jülich high-speed chopper and a millisecond shutter isolated single X-ray pulses from the high-frequency pulse train.

A solution of horse heart MbCO was prepared as follows. Powder of horse heart Mb was dissolved in a 100-mM sodium phosphate buffer at a neutral pH, resulting in an 8-mM solution. The horse heart Mb solution was reduced by adding sodium dithionite of 10 mM concentration and bubbled by CO gas for over 30 min to form horse heart MbCO. The sample solution was prepared just prior to the time-resolved X-ray solution scattering experiment. An aliquot of the resulting horse heart MbCO solution was injected into a 1-mm diameter X-ray capillary and immediately sealed with an UV glue to avoid gas exchange while CO gas was continuously purged into the capillary.

The horse heart MbCO sample was excited by ~2-ps-long laser pulses at 532 nm generated from a picosecond laser system. Femtosecond pulse train at 780 nm generated from a Ti: Sapphire oscillator seeded a picosecond Ti: Sapphire amplifier. TOPAS optical parametric amplifier converted the output of the amplifier to 532 nm. To minimize the laser-polarization-induced anisotropy [22], the circularly polarized laser pulse of ~48 μJ was used with a spot size of $0.11 \times 0.55$ mm$^2$ (horizontal × vertical, FWHM) at the sample position, producing an energy density of 1.0 mJ/mm$^2$. The sample was excited by a laser pulse from the top and maintained at 22 °C with a cold nitrogen stream. The X-ray pulse passed 200-μm deep from the top of the capillary in perpendicular geometry. The scattered X-ray pulses by the sample were recorded with a two-dimensional Mar165 CCD detector. To minimize the air scattering, a cone filled with helium gas was inserted between the sample and the CCD detector. To provide a fresh portion of the sample for every pair of X-ray and laser pulses, the linear translational stage was used to translate the capillary containing the sample.

The laser-off images were collected with the X-ray pulse arriving 5 μs earlier than the laser pulse (that is, −5 μs) in order to measure the contribution of (ground) unexcited state while ensuring the same average temperature of the sample solution. These laser-off images were used as a reference for generating difference scattering images.

Typically, a laser-off image was measured after every 3 laser-on images to counterbalance the slow drifts of the X-ray intensity in the beamline. To achieve sufficient signal-to-noise ratio, ~50 images were collected at each time delay. The laser-on images were measured at the following (nominal) time delays: −130 ps, −120 ps, −110 ps, −100 ps, −90 ps, −80 ps, −70 ps, −60 ps, −50 ps, −40 ps, −30 ps, −20 ps, −10 ps, 0 ps, 10 ps, 20 ps, 30 ps, 40 ps, 50 ps, 60 ps, 70 ps, 80 ps, 100 ps, 120 ps, 140 ps, 160 ps, and 10 ms. The time step of 10 ps (or 20 ps at later time delays) is much smaller than the typical values used in previous studies.

Two-dimensional X-ray solution scattering images were azimuthally averaged to generate one-dimensional X-ray solution scattering curves. The photo-induced scattering intensity changes are smaller than a few percent of the static scattering intensity and thus a careful normalization is needed to calculate correct

photo-induced scattering intensity difference. As a normalization reference, we used the isosbestic point of the water scattering curves with respect to temperature change ($q = 2.07$ Å$^{-1}$) so that the difference scattering intensity at this $q$ value is zero. By taking the differences between the laser-on scattering curves measured at positive time delays and the reference scattering curve measured at $-5$ μs (laser-off), the time-resolved difference X-ray solution scattering curves, $q\Delta S(q, t)$ was obtained. The difference scattering curves, $q\Delta S(q, t)$, following photoexcitation of horse heart Mb solution are shown in Fig. 2.

## 3. Results and discussion

To determine (1) how many structurally distinguishable intermediates of horse heart Mb are formed in the time range of our interest and (2) how fast each intermediate is formed, we performed the singular value decomposition (SVD) analysis of the experimental data in the $q$ range of 0.15–1.0 Å$^{-1}$ and the time range from $-130$ ps to 160 ps. Detailed description of the SVD analysis can be found in our previous publications [21,24–26]. In brief, from the time-resolved X-ray solution scattering curves acquired at various time delays, we produced an $n_q \times n_t$ matrix $\boldsymbol{A}_{exp}(q, t)$, where $n_q$ is the number of $q$ points in the scattering curve at a given time-delay point and $n_t$ is the number of time delay points. For the data matrix $\boldsymbol{A}_{exp}(q, t)$ measured in this work, $n_q$ and $n_t$ are 416 and 26, respectively. Then, we decomposed the matrix $\boldsymbol{A}_{exp}(q, t)$ into three matrices ($\boldsymbol{U}_{exp}(q)$, $\boldsymbol{S}_{exp}$, and $\boldsymbol{V}_{exp}(t)$) while obeying the relationship:

$$\mathbf{A}_{exp}(q,t) = \mathbf{U}_{exp}(q)\mathbf{S}_{exp}\mathbf{V}_{exp}(t)^T \quad (1)$$

where $\boldsymbol{U}_{exp}(q)$ is a $n_q \times n_t$ matrix whose column vectors correspond to time-independent $q$ spectra of $\boldsymbol{A}_{exp}(q, t)$ (left singular vectors; lSVs), $\boldsymbol{S}_{exp}$ is a $n_t \times n_t$ diagonal matrix whose diagonal elements correspond to singular values of $\boldsymbol{A}_{exp}(q, t)$, and $\boldsymbol{V}_{exp}(t)$ is a $n_t \times n_t$ matrix whose column vectors correspond to amplitude changes of $\boldsymbol{U}_{exp}(q)$ as a function of time (right singular vectors; rSVs). The matrices $\boldsymbol{U}_{exp}(q)$ and $\boldsymbol{V}_{exp}(t)$ obey the following relationship:

$$\mathbf{U}_{exp}(q)\mathbf{U}_{exp}(q)^T = \mathbf{V}_{exp}(t)\mathbf{V}_{exp}(t)^T = \mathbf{I}_{n_t} \quad (2)$$

where $\boldsymbol{I}_{nt}$ is the identity matrix. Since the singular values of $\boldsymbol{S}_{exp}$ are ordered so that $s_1 \geqslant s_2 \geqslant \ldots \geqslant s_{nt} > 0$, both lSVs and rSVs on more left have larger contributions to the data. Accordingly, we can extract time-independent scattering intensity components from the lSVs and time-dependent change of their amplitudes from the rSVs.

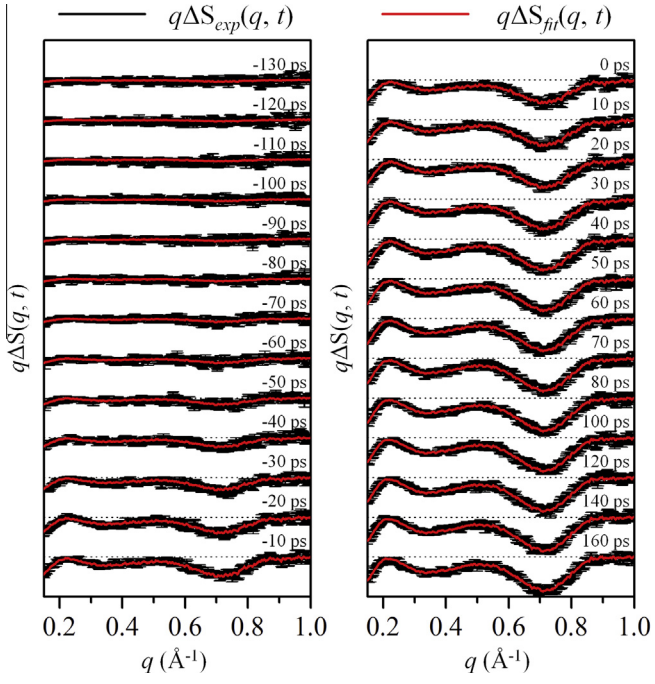


**Fig. 2.** Time-resolved difference X-ray solution scattering curves, $q\Delta S(q, t)$, measured for a solution sample of horse heart MbCO after the ligand photodissociation. The (nominal) time delay after the photodissociation is indicated above each curve. Experimental data (black) are compared with theoretical data (red). See the text for details. (For interpretation of the references to colour in this figure legend, the reader is referred to the web version of this article.)

The singular values and autocorrelation values of the singular vectors shown in Fig. 3 suggest that only the first two singular components are significant enough to represent the experimental data, while the contributions from the third singular component and beyond are insignificant. In other words, only two structurally distinguishable intermediates are formed in the time range investigated in this work. Then, we extracted the relaxation times of rSVs to determine the structural dynamics of Mb. If the temporal width of X-ray pulse is shorter than the time scale of the dynamics of our interest, the relaxation times of rSVs can be determined simply by globally fitting the rSVs with multiple exponentials. However, the X-ray pulse duration in this work is longer than or comparable to the dynamics of our interest, and therefore we need to deconvolute the temporal profile of the X-ray pulse from the measured data in order to determine the relaxation times accurately.In theory, our experimental data, $\boldsymbol{A}_{exp}(q, t)$, presented in this work can be expressed as a convolution [27]:

$$\mathbf{A}_{exp}(q,t) = \mathbf{A}_{inst}(q, t-t_0) \otimes I_{X-ray}(t-t_0) \quad (3)$$

where $\boldsymbol{A}_{inst}(q, t)$ is $n_q \times n_t$ matrix containing the instantaneous response of the solution sample, $I_{X\text{-}ray}(t)$ is the temporal intensity profile of X-ray pulse, and $t_0$ is the actual time-zero value of the measurement. According to Eq. (1), the following relationship also holds:

$$\mathbf{V}_{exp}(t) = \mathbf{V}_{inst}(t-t_0) \otimes I_{X-ray}(t-t_0) \quad (4)$$

where $\boldsymbol{V}_{inst}(t)$ is a $n_t \times n_t$ matrix whose column vectors correspond to the amplitude changes of $\boldsymbol{U}_{exp}(q)$ as a function of time (right singular vectors; rSVs) in case that an infinitely short X-ray pulse is used. Because only the first two singular components contribute significantly to the data, we defined new matrices ($\boldsymbol{U}'_{exp}(q)$, $\boldsymbol{S}'_{exp}$, and $\boldsymbol{V}'_{exp}(t)$) to remove the contributions of insignificant singular components. $\boldsymbol{U}'_{exp}(q)$ is a $n_q \times 2$ matrix containing only the first two left singular vectors of $\boldsymbol{U}_{exp}(q)$, $\boldsymbol{S}'_{exp}$, is a $2 \times 2$ matrix containing only the first two singular values of $\boldsymbol{S}_{exp}$, and $\boldsymbol{V}'_{exp}(t)$ is a $2 \times n_t$ matrix containing only the first two right singular vectors of $\boldsymbol{V}_{exp}(t)$. We used only these matrices to extract the structural dynamics of the protein transition. From Eq. (4), we can obtain the following relationship:

$$\mathbf{V}'_{exp}(t) = \mathbf{V}'_{inst}(t-t_0) \otimes I_{X-ray}(t-t_0) \quad (5)$$

where $\boldsymbol{V}'_{inst}(t)$ is an $2 \times n_t$ matrix containing only the first two column vectors of $\boldsymbol{V}_{inst}(t)$. We can model the column vectors of $\boldsymbol{V}'_{inst}(t)$ by a sum of multiple exponentials sharing common relaxation times. Then, we optimized the coefficients and the relaxation times of the exponentials as well as the actual time zero, $t_0$, by minimizing the discrepancy (i.e. chi-square value) between $\boldsymbol{V}'_{exp}(t)$ and the convolution of $\boldsymbol{V}'_{inst}(t-t_0)$ and $I_{X\text{-}ray}(t-t_0)$. However, standard deviations for $\boldsymbol{V}'_{exp}(t)$, which are needed for the optimization described above, are not available from our experimental data and thus we instead used the following method to optimize $\boldsymbol{V}'_{inst}(t)$. According to Eqs. (1) and (5), the following relationship holds:

$$\mathbf{A}_{exp}(q,t) = \mathbf{U}'_{exp}(q)\mathbf{S}'_{exp}\left(\mathbf{V}'_{\mathbf{inst}}(\mathbf{t}-\mathbf{t_0}) \otimes \mathbf{I}_{\mathbf{X-ray}}(\mathbf{t}-\mathbf{t_0})\right)^T \quad (6)$$

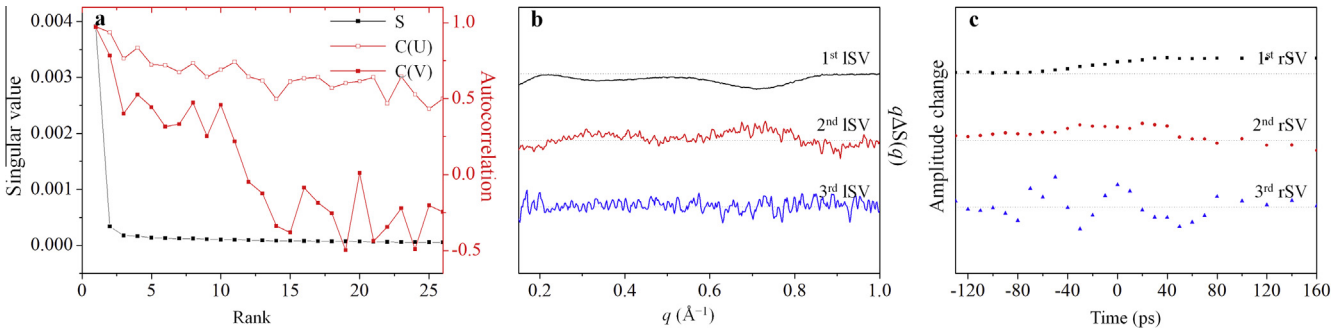


**Fig. 3.** Result of the SVD analysis. (a) Singular values (black solid squares) and autocorrelation values of left singular vectors (red open squares) and right singular vectors (red solid squares) obtained from the SVD analysis of the experimental data, (b) the first three left singular vectors, (c) the first three right singular vectors. (For interpretation of the references to colour in this figure legend, the reader is referred to the web version of this article.)

The matrix $\boldsymbol{V}'_{inst}(t)$ was optimized by minimizing the discrepancy between the experimental data and the right term in Eq. (6) using the Minuit package.

From the deconvolution described above (see Fig. 4), we found that the column vectors of $\boldsymbol{V}'_{inst}(t)$ were fit by an exponential with the time constant of 70 ± 20 ps and a constant offset (that is, a slow decay beyond the time range up to 160 ps). The actual time zero was off from the nominal time zero by 10 ± 2 ps, and this discrepancy is within the RMS jitter of our measurement [52]. Based on the results of SVD analysis and the deconvolution, we can reason the origin of the 70-ps kinetic component. As mentioned above, the SVD analysis identifies two structurally distinguishable intermediates in the time range up to 160 ps. According to previous studies on horse heart MbCO using various time-resolved optical spectroscopies, an intermediate called the **B** state is formed in only several picoseconds [41–45]. Here, the **B** state refers to the Mb intermediate with the photodissociated CO ligands located at the primary docking site [21,40]. We can therefore infer that, among the two intermediates identified by the SVD analysis, the earlier one corresponds to the **B** state. Accordingly, the 70-ps component must represent the transition from the **B** state to the later intermediate. The later intermediate is likely to be the **C** state because no other intermediate has been identified between the **B** and **C** states in previous studies [21,40]. Here, the **C** state refers to the Mb intermediate with the photodissociated CO ligands located in a cavity inside the protein. In previous studies on horse heart MbCO, a kinetic component on a similar time scale was observed using time-resolved infrared spectroscopy (83 ps) [42] and time-resolved circular dichroism (50 ps) [45] and was assigned to tertiary structural change induced by the local structural stress of the proximal histidine around the heme.

Meanwhile, in our previous study on horse heart MbCO using time-resolved X-ray solution scattering with the time resolution of 100 ps [21], it was shown that the **B** state transforms to the **C** state in 360 ps. This kinetic component for the **B**-to-**C** transition is much slower than the 70-ps kinetic component found in this work and is likely to correspond to the slow decay described by a constant offset in the fits of $\boldsymbol{V}'_{inst}(t)$ in Fig. 4. Considering that the two kinetic components on different time scales (70 ps and 360 ps) can be assigned to the **B**-to-**C** transition, we can infer that the **B**-to-**C** transition occurs in a biphasic manner with the time constants of 70 ps and 360 ps. In fact, we recently investigated the structural dynamics of sperm whale MbCO using time-resolved X-ray solution scattering and revealed that the **B**-to-**C** transition occurs biphasically with the time constants of 460 ps and 3.6 ns [26]. In analogy to the case of sperm whale MbCO, it is plausible that both the 70-ps component of the present work and the 360-ps component of our previous work [21] account for the biphasic **B**-to-**C** transition occurring in horse heart MbCO as well. However, determination of the optimum kinetic model for horse heart MbCO is beyond the scope of this paper and will be further investigated by our group in the near future.

In addition to $\boldsymbol{V}'_{inst}(t)$, we also retrieved time-resolved difference scattering curves, $\boldsymbol{A}'_{inst}(q, t)$, representing the instantaneous

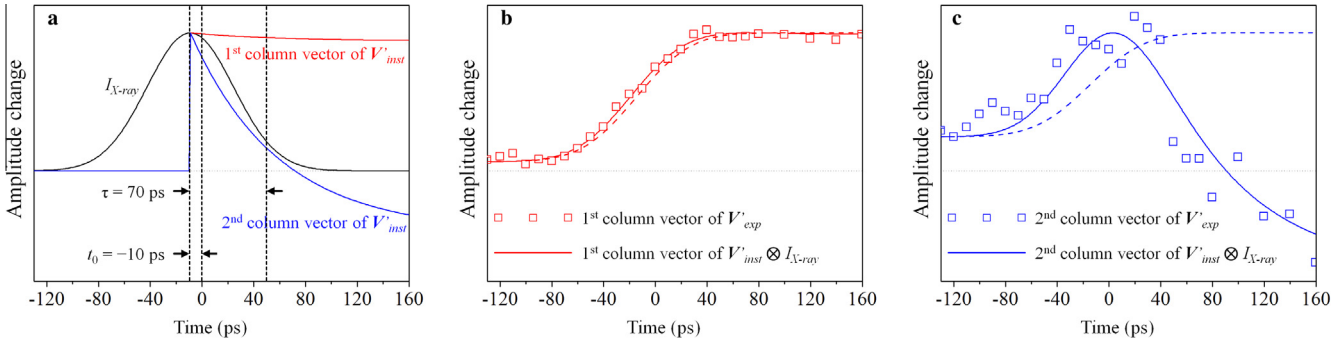


**Fig. 4.** (a) In the deconvolution, the temporal profile of X-ray intensity, $I_{X\text{-ray}}(t)$ (black solid line), was modeled by a Gaussian function with 80 ps FWHM width, which is a typical temporal width of the top-up mode at the APS. The column vectors of $\boldsymbol{V}'_{inst}(t)$ were modeled by a sum of multiple exponentials. The actual time zero, $t_0$, as well as the coefficients and the relaxation times of the exponentials were used as fitting parameters to retrieve $\boldsymbol{V}'_{inst}(t)$. By minimizing the discrepancy between the experimental and theoretical difference scattering curves, we obtained the optimized first column vector of $\boldsymbol{V}'_{inst}(t)$ (red solid line) and the optimized second column vector of $\boldsymbol{V}'_{inst}(t)$ (blue solid line). These two column vectors were fit by an exponential with the time constant of 70 ps and a constant offset. The actual time zero was found to be off from the nominal time-zero by about 10 ps, (b) the first column vector of $\boldsymbol{V}'_{exp}(t)$ (red open squares) is compared with the convolution (red solid line) of the optimized first column vector of $\boldsymbol{V}'_{inst}(t)$ and $I_{X\text{-ray}}(t)$. The integration of $I_{X\text{-ray}}(t)$ over time (red dashed line) is shown together to represent the instrument response without any contribution from the sample, (c) the second column vector of $\boldsymbol{V}'_{exp}(t)$ (blue open squares) is compared with the convolution (blue solid line) of the optimized second column vector of $\boldsymbol{V}'_{inst}(t)$ and $I_{X\text{-ray}}(t)$. The integration of $I_{X\text{-ray}}(t)$ over time (blue dashed line) is shown together to represent the instrument response without any contribution from the sample. (For interpretation of the references to colour in this figure legend, the reader is referred to the web version of this article.)

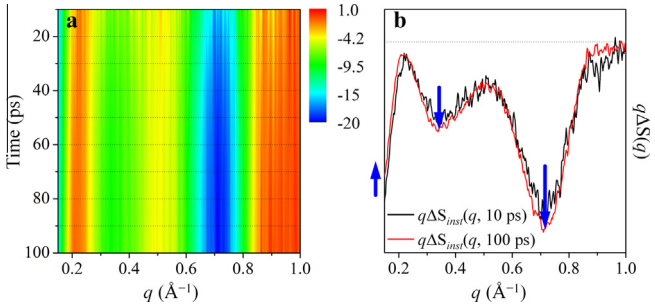


**Fig. 5.** Time-resolved difference scattering curves, $\boldsymbol{A}'_{inst}(q,t)$, corresponding to the instantaneous response of the solution sample. (a) Time-resolved difference scattering curves, $q\Delta S(q,t)$, with the X-ray temporal intensity profile deconvoluted and (b) their cross sections at two representative time delays, 10 ps and 100 ps. Blue arrows indicate $q$ values where the intensity difference between the scattering curves at the two time delays is significant.

response of the solution sample by using the following equation (see Fig. 5):

$$\mathbf{A}'_{inst}(q,t) = \mathbf{U}'_{exp}(q)\mathbf{S}'_{exp}\mathbf{V}'_{inst} \tag{7}$$

Because the local protein structure around the heme changes on the time scale shorter than 10 ps [41–45], only the curves later than 10 ps are shown. We can clearly see that the curve at 10 ps and the one at 100 ps are significantly different from each other, reflecting the structural change occurring in the time range between 10 and 100 ps. In particular, as the time evolves, the negative peak at low $q$ decreases (that is, becomes less negative) while the negative peaks at 0.35 $Å^{-1}$ and 0.7 $Å^{-1}$ increase (that is, become more negative). The structural evolution of the protein in this time range will be further investigated by our group in the near future.

## 4. Summary

In this work, we investigated sub-100-ps structural dynamics of horse heart MbCO after ligand photodissociation by combining time-resolved X-ray solution scattering and the time-slicing scheme. Improved time resolution via the time-slicing measurement allowed us to reveal the 70-ps kinetic component, which is ascribed to the **B**-to-**C** transition of Mb. In the near future, femtosecond X-ray pulses from the XFEL will open opportunities to study the dynamics of protein structural transitions at the earliest stage.

## Acknowledgements

We acknowledge BioCARS staffs for support and helpful discussions. This work was supported by Institute for Basic Science (IBS) [CA1401-01]. Use of the BioCARS Sector 14 at the APS was supported by the National Institutes of Health (NIH) National Institute of General Medical Sciences grant P41GM103543. The time-resolved set up at Sector 14 was funded in part through collaboration with P. Anfinrud (NIH/NIDDK) through the Intramural Research Program of the NIDDK. Use of the APS was supported by the US Department of Energy, Basic Energy Sciences, Office of Science, under Contract No. DE-AC02-06CH11357.

## References

[1] H. Ihee, M. Lorenc, T.K. Kim, Q.Y. Kong, M. Cammarata, J.H. Lee, S. Bratos, M. Wulff, Science 309 (2005) 1223.
[2] A. Plech, M. Wulff, S. Bratos, F. Mirloup, R. Vuilleumier, F. Schotte, P.A. Anfinrud, Phys. Rev. Lett. 92 (2004) 125505.
[3] J. Davidsson, J. Poulsen, M. Cammarata, P. Georgiou, R. Wouts, G. Katona, F. Jacobson, A. Plech, M. Wulff, G. Nyman, R. Neutze, Phys. Rev. Lett. 94 (2005) 245503.
[4] T.K. Kim, M. Lorenc, J.H. Lee, M. Lo Russo, J. Kim, M. Cammarata, Q. Kong, S. Noel, A. Plech, M. Wulff, H. Ihee, Proc. Natl. Acad. Sci. U.S.A. 103 (2006) 9410.
[5] M. Cammarata, M. Lorenc, T.K. Kim, J.H. Lee, Q.Y. Kong, E. Pontecorvo, M. Lo Russo, G. Schiro, A. Cupane, M. Wulff, H. Ihee, J. Chem. Phys. 124 (2006) 124504.
[6] J.H. Lee, K.H. Kim, T.K. Kim, Y. Lee, H. Ihee, J. Chem. Phys. 125 (2006) 174504.
[7] Q. Kong, M. Wulff, J.H. Lee, S. Bratos, H. Ihee, J. Am. Chem. Soc. 129 (2007) 13584.
[8] J.H. Lee, J. Kim, M. Cammarata, Q. Kong, K.H. Kim, J. Choi, T.K. Kim, M. Wulff, H. Ihee, Angew. Chem. Int. Ed. 47 (2008) 1047.
[9] J.H. Lee, T.K. Kim, J. Kim, Q. Kong, M. Cammarata, M. Lorenc, M. Wulff, H. Ihee, J. Am. Chem. Soc. 130 (2008) 5834.
[10] Q. Kong, J.H. Lee, A. Plech, M. Wulff, H. Ihee, M.H. Koch, Angew. Chem. Int. Ed. 47 (2008) 5550.
[11] M. Cammarata, M. Levantino, F. Schotte, P.A. Anfinrud, F. Ewald, J. Choi, A. Cupane, M. Wulff, H. Ihee, Nat. Methods 5 (2008) 881.
[12] H. Ihee, Acc. Chem. Res. 42 (2009) 356.
[13] T.K. Kim, J.H. Lee, M. Wulff, Q.Y. Kong, H. Ihee, Chem. Phys. Chem. 10 (2009) 1958.
[14] K. Haldrup, M. Christensen, M. Cammarata, Q. Kong, M. Wulff, S.O. Mariager, K. Bechgaard, R. Feidenhans'l, N. Harrit, M.M. Nielsen, Angew. Chem. Int. Ed. 48 (2009) 4180.
[15] M. Christensen, K. Haldrup, K. Bechgaard, R. Feidenhans'l, Q. Kong, M. Cammarata, M. Lo Russo, M. Wulff, N. Harrit, M.M. Nielsen, J. Am. Chem. Soc. 131 (2009) 502.
[16] Q. Kong, J.H. Lee, M. Lo Russo, T.K. Kim, M. Lorenc, M. Cammarata, S. Bratos, T. Buslaps, V. Honkimaki, H. Ihee, M. Wulff, Acta. Crystallogr. A 66 (2010) 252.
[17] Q. Kong, J.H. Lee, K.H. Kim, J. Kim, M. Wulff, H. Ihee, M.H. Koch, J. Am. Chem. Soc. 132 (2010) 2600.
[18] S. Jun, J.H. Lee, J. Kim, K.H. Kim, Q. Kong, T.K. Kim, M. Lo Russo, M. Wulff, H. Ihee, Phys. Chem. Chem. Phys. 12 (2010) 11536.
[19] S. Westenhoff, E. Malmerberg, D. Arnlund, L. Johansson, E. Nazarenko, M. Cammarata, J. Davidsson, V. Chaptal, J. Abramson, G. Katona, A. Menzel, R. Neutze, Nat. Methods 7 (2010) 775.
[20] H.S. Cho, N. Dashdorj, F. Schotte, T. Graber, R. Henning, P. Anfinrud, Proc. Natl. Acad. Sci. U.S.A. 107 (2010) 7281.
[21] K.H. Kim, K.Y. Oang, J. Kim, J.H. Lee, Y. Kim, H. Ihee, Chem. Commun. 47 (2011) 289.
[22] J. Kim, K.H. Kim, J.G. Kim, T.W. Kim, Y. Kim, H. Ihee, J. Phys. Chem. Lett. 2 (2011) 350.
[23] J. Kim, J.H. Lee, J. Kim, S. Jun, K.H. Kim, T.W. Kim, M. Wulff, H. Ihee, J. Phys. Chem. A 116 (2012) 2713.
[24] K.H. Kim, S. Muniyappan, K.Y. Oang, J.G. Kim, S. Nozawa, T. Sato, S.Y. Koshihara, R. Henning, I. Kosheleva, H. Ki, Y. Kim, T.W. Kim, J. Kim, S. Adachi, H. Ihee, J. Am. Chem. Soc. 134 (2012) 7001.
[25] T.W. Kim, J.H. Lee, J. Choi, K.H. Kim, L.J. van Wilderen, L. Guerin, Y. Kim, Y.O. Jung, C. Yang, J. Kim, M. Wulff, J.J. van Thor, H. Ihee, J. Am. Chem. Soc. 134 (2012) 3145.
[26] K.Y. Oang, J.G. Kim, C. Yang, T.W. Kim, Y. Kim, K.H. Kim, J. Kim, H. Ihee, J. Phys. Chem. Lett. 5 (2014) 804.
[27] J.H. Lee, M. Wulff, S. Bratos, J. Petersen, L. Guerin, J.C. Leicknam, M. Carnmarata, Q. Kong, J. Kim, K.B. Moller, H. Ihee, J. Am. Chem. Soc. 135 (2013) 3255.
[28] K.H. Kim, H. Ki, K.Y. Oang, S. Nozawa, T. Sato, J. Kim, T.K. Kim, J. Kim, S.I. Adachi, H. Ihee, Chem. Phys. Chem. (2013) 3687.
[29] L. Salassa, E. Borfecchia, T. Ruiu, C. Garino, D. Gianolio, R. Gobetto, P.J. Sadler, M. Cammarata, M. Wulff, C. Lamberti, Inorg. Chem. 49 (2010) 11240.
[30] J. Vincent, M. Andersson, M. Eklund, A.B. Wohri, M. Odelius, E. Malmerberg, Q. Kong, M. Wulff, R. Neutze, J. Davidsson, J. Chem. Phys. 130 (2009) 154502.
[31] K. Haldrup, T. Harlang, M. Christensen, A. Dohn, T.B. van Driel, K.S. Kjaer, N. Harrit, J. Vibenholt, L. Guerin, M. Wulff, M.M. Nielsen, Inorg. Chem. 50 (2011) 9329.
[32] E. Malmerberg, Z. Omran, J.S. Hub, X. Li, G. Katona, S. Westenhoff, L.C. Johansson, M. Andersson, M. Cammarata, M. Wulff, D. van der Spoel, J. Davidsson, A. Specht, R. Neutze, Biophys. J. 101 (2011) 1345.
[33] S. Ibrahimkutty, P. Wagener, A. Menzel, A. Plech, S. Barcikowski, Appl. Phys. Lett. 101 (2012) 103104.
[34] K. Haldrup, G. Vanko, W. Gawelda, A. Galler, G. Doumy, A.M. March, E.P. Kanter, A. Bordage, A. Dohn, T.B. van Driel, K.S. Kjaer, H.T. Lemke, S.E. Canton, J. Uhlig, V. Sundstrom, L. Young, S.H. Southworth, M.M. Nielsen, C. Bressler, J. Phys. Chem. A 116 (2012) 9878.
[35] S. Ibrahimkutty, J. Kim, M. Cammarata, F. Ewald, J. Choi, H. Ihee, A. Plech, ACS Nano 5 (2011) 3788.
[36] A. Plech, V. Kotaidis, A. Siems, M. Sztucki, Phys. Chem. Chem. Phys. 10 (2008) 3888.
[37] K.H. Kim, J.H. Lee, J. Kim, S. Nozawa, T. Sato, A. Tomita, K. Ichiyanagi, H. Ki, J. Kim, S. Adachi, H. Ihee, Phys. Rev. Lett. 110 (2013) 165505.
[38] K.H. Kim, J. Kim, J.H. Lee, H. Ihee, Struct. Dyn. 1 (2014) 011301.
[39] K. Chu, J. Vojtchovsky, B.H. McMahon, R.M. Sweet, J. Berendzen, I. Schlichting, Nature 403 (2000) 921.
[40] Y. Nishihara, M. Sakakura, Y. Kimura, M. Terazima, J. Am. Chem. Soc. 126 (2004) 11877.
[41] L. Richard, L. Genberg, J. Deak, H.L. Chiu, R.J.D. Miller, Biochemistry 31 (1992) 10703.
[42] M.H. Lim, T.A. Jackson, P.A. Anfinrud, Proc. Natl. Acad. Sci. U.S.A. 90 (1993) 5801.
[43] G.D. Goodno, V. Astinov, R.J.D. Miller, J. Phys. Chem. A 103 (1999) 10630.

[44] Y. Mizutani, T. Kitagawa, J. Phys. Chem. B 105 (2001) 10992.
[45] T. Dartigalongue, F. Hache, Chem. Phys. Lett. 415 (2005) 313.
[46] Y.O. Jung, J.H. Lee, J. Kim, M. Schmidt, K. Moffat, V. Srajer, H. Ihee, Nat. Chem. 5 (2013) 212.
[47] F. Schotte, M.H. Lim, T.A. Jackson, A.V. Smirnov, J. Soman, J.S. Olson, G.N. Phillips, M. Wulff, P.A. Anfinrud, Science 300 (2003) 1944.
[48] H. Ihee, S. Rajagopal, V. Srajer, R. Pahl, S. Anderson, M. Schmidt, F. Schotte, P.A. Anfinrud, M. Wulff, K. Moffat, Proc. Natl. Acad. Sci. U.S.A. 102 (2005) 7145.
[49] J.E. Knapp, R. Pahl, V. Srajer, W.E. Royer Jr., Proc. Natl. Acad. Sci. U.S.A. 103 (2006) 7649.
[50] J.E. Knapp, R. Pahl, J. Cohen, J.C. Nichols, K. Schulten, Q.H. Gibson, V. Srajer, W.E. Royer Jr., Structure 17 (2009) 1494.
[51] F. Schotte, H.S. Cho, J. Soman, M. Wulff, J.S. Olson, P.A. Anfinrud, Chem. Phys. 422 (2013) 98.
[52] T. Graber, S. Anderson, H. Brewer, Y.S. Chen, H.S. Cho, N. Dashdorj, R.W. Henning, I. Kosheleva, G. Macha, M. Meron, R. Pahl, Z. Ren, S. Ruan, F. Schotte, V.S. Rajer, P.J. Viccaro, F. Westferro, P. Anfinrud, K. Moffat, J. Synchrotron Radiat. 18 (2011) 658.